REVISION 2

The effect of halogens (F, Cl) on the near-liquidus crystallinity of a hydrous trachyte melt

Word count: 7852

Yves Feisel[a,*], Jonathan M. Castro[a], Christoph Helo[a], Donald B. Dingwell[b,c]

[a] Institute of Geosciences, Johannes Gutenberg-Universität Mainz, 55128 Mainz, Germany

[b] Department für Geo- und Umweltwissenschaften, Ludwig-Maximilians-Universität München, 80333 München, Germany

[c] Gutenberg Research College, Johannes Gutenberg-Universität Mainz, 55128 Mainz, Germany

[*]corresponding author: yfeise02@uni-mainz.de

Abstract

The effect of F and Cl on the liquidus temperature of a hydrous (~3.5 – 4 wt% H_2O) trachytic melt (~66 wt% SiO_2) at 925 to 990 °C and at 100 MPa has been experimentally investigated. We employed a novel disequilibrium approach involving diffusion couple experiments with the two diffusion couple end-members differing solely in halogen concentrations. A shift of the liquidus temperature by ~50 °C was observed between a halogen-poor and halogen-enriched melt. Each experiment spanned the entire range of F and Cl concentrations between the two endmember compositions. We determined the halogen concentrations at the transition from crystal-bearing to crystal-free melt. These concentrations correspond to the liquidus halogen concentrations of

the melt at each experimental temperature. We demonstrate that there is a limiting halogen concentration (~0.19 – 0.52 wt% F; ~0.07 – 0.24 wt% Cl), below which the melt crystallizes spherulitic clinopyroxene during heating to the run temperature. At high temperature, upon diffusion of F and Cl into the halogen-poor melt, those crystals dissolve, leaving behind a dissolution front parallel to the diffusion interface. We propose that the dissolution is a consequence of F and Cl complexing with some of the main cationic components of clinopyroxene (Mg, Fe, Ca) thereby destabilizing this phase. Thus, the experimental dissolution of clinopyroxene is a manifestation of a liquidus depression caused by increased halogen content. Our results show that the liquidus shifts at a rate of ~1575(379) K/mol% of F and Cl in the melt, which is a minimum estimate, assuming both halogens equally drive dissolution. This liquidus depression is valid for a range of halogen concentrations (~0.06 – 0.87 wt% F; ~0.06 – 0.36 wt% Cl) and the experimental temperatures. Our findings illustrate that the degassing of halogens during or prior to an eruption can enhance crystallization in the melt and therefore influence magma physical properties that may ultimately affect eruption style.

Keywords: halogens; liquidus depression; phase equilibria; diffusion couple; crystal dissolution

1 Introduction

Volatile species (H_2O, CO_2, F, Cl, S etc.) are important constituents of natural silicate melts and play a crucial role in determining melt properties (e.g., viscosity, density) and a magma's phase assemblage (e.g., crystallinity, bubble content). Hence they can ultimately control the style of

volcanic eruptions (e.g., Gonnermann and Manga 2007). Despite their typically moderate concentrations in magmas, compared to other major volatiles such as H_2O or CO_2, F and Cl may reach abundances of 100's of ppms up to few weight percent and, thus may exert significant effects on their own (e.g., Aiuppa et al. 2009; Dolejs and Zajacz 2018). For example, F has long been known to decrease melt viscosity in silica-rich melts in a manner qualitatively similar to that of H_2O (Dingwell et al. 1985; Dingwell and Hess 1998; Zimova and Webb 2007; Giordano et al. 2008). By contrast, although the details of the effect of Cl on melt viscosity vary, it has been shown that Cl cannot decrease viscosity with the same efficiency as F and that the effect on viscosity is dependent on the melt composition (Hirayama and Camp 1969; Dingwell and Hess 1998; Zimova and Webb 2006; Webb et al. 2014). The solubility of Cl in silicate melts has been demonstrated to be roughly an order of magnitude higher in basaltic melts than in rhyolitic compositions and increases with the availability of Mg, Ca, Na, Fe, K, Al and F in the melt, while decreasing with the concentration of network-forming Si (Carroll and Webster 1994; Signorelli and Carroll 2002; Webster and De Vivo 2002; Chevychelov et al. 2008; Webster et al. 2015, 2018; Thomas and Wood 2021). These findings are consistent with spectroscopy-based investigations which indicate a preferred complexing of Cl with Ca, Mg and Fe (Zimova and Webb 2006; Evans et al. 2008; Webb et al. 2014; Bell and Webster 2015). F solubility has also been demonstrated to correlate with the concentration of Ca and Mg where they assume the role of network-modifiers and with increasing peralkalinity (molar [Na+K+Ca] / [Al] > 1; e.g., Koster van Groos and Wyllie 1968; Foley et al. 1986b, 1986a; Mysen et al. 2004; Brey et al. 2009). Additionally, F dissolution in silicate melt increases in peraluminous melts with excess network-modifying Al in 4-fold coordination (Webster et al., 2018 and references therein). F has been shown to replace bridging oxygens (Schaller et al. 1992; Dolejš and Zajacz 2018) and form

complexes with Ca, Mg or Na, as well as Al in 4-fold or 6-fold coordination (e.g., Karpukhina et al., 2007; Mysen et al., 2004; Zeng and Stebbins, 2000).

The effects of halogens on phase equilibria include significant depression of liquidus temperatures by F in both basaltic (Filiberto et al. 2012) and felsic melts (e.g., Wyllie and Tuttle 1961; Koster van Groos and Wyllie 1968; Manning 1981; Dolejš and Baker 2007a, 2007b). Of the studies available for the effect of Cl on phase equilibria, the majority indicate a decrease of the solidus temperature depending on the melt composition and Cl concentration (e.g., Wyllie and Tuttle 1964; Koster van Groos and Wyllie 1969). Recent studies on the effects of Cl on liquidus relations in basaltic melts showed a significant Cl-composition-dependent depression of the isobaric liquidus, defined by the first occurrence of olivine or pyroxene depending on the pressure (Filiberto and Treiman 2009; Filiberto et al. 2014; Farcy et al. 2016). The addition of Cl to a hydrous rhyodacitic melt was shown to exert a strong influence on the $Fe^{3+}/\sum Fe$ ratio, resulting in increased magnetite solubility (Bell and Webster, 2015). While some of the above studies were carried out on simplified model systems (e.g., Wyllie and Tuttle 1961, 1964; Koster van Groos and Wyllie 1968, 1969; Manning 1981; Swanson and Fenn 1992; Dolejš and Baker 2007a, 2007b; Evans et al. 2008; Clarke et al. 2009), most recent work was done using natural compositions and therefore provide an extensive but not yet complete base of knowledge of the effects of halogens on a broad range of melt compositions (e.g., Webster and De Vivo 2002; Bell and Simon 2011; Filiberto et al. 2012, 2014; Webb et al. 2014; Bell and Webster 2015; Webster et al. 2015; Farcy et al. 2016; Thomas and Wood 2021). For more comprehensive summaries of the effects of halogens on silicate melt properties, see reviews by Aiuppa et al. (2009), Dolejs and Zajacz, (2018), and Webster et al. (2018).

93

94 Here we investigate the effects of fluorine and chlorine on the crystallization behavior of a
95 hydrous trachytic melt. During the investigation of the diffusivity of F and Cl in silicic melts
96 (e.g., Feisel et al. 2019; in preparation) we have observed the strong effects of the halogen
97 concentration gradient on the phase equilibria in this melt system. Below, we determine the
98 halogen concentrations at the transition from crystal-bearing to crystal-free assemblages of
99 hydrous trachytic melt. We show that very low F and Cl concentrations added to the melt phase
100 (100's of ppm) lead to a first-order effect on the crystallization properties and may therefore
101 influence the state and behavior of these systems during a volcanic eruption or during hot
102 volcanic deposition processes.

103

104

105 ## 2 Methods

106

107 ### 2.1 Experimental procedure

108 Synthesis of the starting materials was conducted at the LMU Munich. Experimental glasses
109 were synthesized from natural lava of the obsidian flow of the 2011 eruption of Cordón Caulle,
110 Chile (e.g., Alloway et al., 2015; Castro et al., 2016, 2013; Schipper et al., 2013). In a first step
111 ca. 800 g of the powdered lava was melted in a large Pt crucible (~10 x 4 cm) at high
112 temperatures (1450-1500 °C) for ~4 days to drive off all volatiles and to homogenize the melt.
113 During the synthesis, the melt was stirred with a Pt-rod (~3 mm diameter) attached to a
114 rheometer to accelerate homogenization and thereby to outrun volatile loss. After stirring, the
115 crucible was removed from the furnace and placed on insulation to cool to a crystal- and bubble-

116 free glass. The resultant glass was split into two aliquots. These aliquots were then remelted to
117 generate the halogen-bearing and halogen-free (hereafter halogen-poor) glasses. Sample CC1,
118 the halogen-bearing glass, was enriched in NaF + NaCl + NaBr + NaI, by adding powders of the
119 sodium halides to achieve ~1 wt% of each halogen in the mixture. Sample CC2, the halogen-
120 poor glass, was enriched in Na_2CO_3, to yield an equivalently Na-enriched halogen-depleted
121 composition (Feisel et al., 2019). During the second synthesis, the melts were again stirred for
122 several days to ensure homogenization before being quenched in air to room temperature.
123
124 Diffusion couple experiments were prepared by introducing the ground glass powders made from
125 samples CC1 and CC2 into 5 mm diameter Pt-tubing (6 mm long). Each capsule was closed on
126 one end with a Pt-lid, and then welded shut and tamped with a tight-fitting metal rod to ensure
127 cylindrical inner geometry. Powder of the halogen-bearing glass was then loaded in the bottom
128 half of the capsule and tamped. An equivalent of ~3.5 wt% H_2O was added to the capsule using a
129 microsyringe. The capsule was then filled with the halogen-poor powder, tamped by hand and
130 another ~3.5 wt% H_2O was added. Tamping of the powders after loading them into the capsule
131 ensured a flat diffusion interface oriented perpendicular to the capsule walls (i.e., perpendicular
132 to the diffusion direction). Finally, a tight-fitting lid was welded to the open end of the capsule
133 using a micro arc welder and tamped into a cylindrical shape with a pressure of ~750 kg. To
134 confirm that the capsules were reliably sealed, they were repeatedly heated to ~120 °C using a
135 heating plate and weighed to confirm no weight loss. Capsules with significant weight loss were
136 discarded. In order to confirm that the diffusion couple experiments were representative of
137 longer term experiments, approaching equilibrium conditions, two additional capsules were

prepared, each containing only one of the starting materials and the equivalent amount of ~3.5 wt% H_2O.

All experiments were conducted at the University of Mainz using horizontal and vertical tube furnaces and Ni-Co-alloy (Rene-41) cold-seal pressure vessels. H_2O was used as the pressure medium and was transmitted by using a Haskel rotary-vane hydraulic pump through a network of high pressure stainless steel tubes. In order to control the oxygen fugacity during an experiment and to prevent convection of H_2O in the vessel, the free space below the sample capsule inside the autoclave was filled with a nickel metal filler-rod (Matthews et al. 2003). The oxidation of the Ni-rod during the experiment controlled the oxygen fugacity in the system close to NNO+1 (e.g., Geschwind and Rutherford 1995; Schmidt and Behrens 2008).

For each experiment, the vessel was placed in the furnace and brought to the target pressure (100 MPa) before increasing the temperature. The pressure was monitored with a pressure transducer and a factory-calibrated Bourdon-tube gauge. Upon heating to the target temperature, the pressure was continuously monitored and adjusted to stay at 100 MPa. Heating took between 40 and 70 minutes to reach the dwell temperature – monitored using a K-type thermocouple being inserted into a bore at the end of the vessel at a point closest to the capsule. The internal thermocouple of the furnace was additionally used to monitor the temperature. Due to the small capsule size (~5 x 6mm) compared to the larger vessel (~39 x 260 mm; ~16 mm wall thickness) and the constant temperature readings of both thermocouples during all runs, we consider the temperature to be constant in the diffusion couple capsule.

In order to preserve the full gradient of halogen concentrations across the diffusion couple the run time was chosen based on the estimated diffusivities of the halogens, and these times varied

from ~1 to ~15 hours depending on the temperature. To evaluate when during the relatively short experimental durations the crystallization and dissolution occurred, a zero-time experiment was conducted whereby the diffusion couple was heated to target temperature (~40 min / 950 °C) and then quenched. Two experiments with pure starting materials were performed simultaneously in the same vessel to ensure the same *P-T* history for both. The duration for these experiments was limited to ~30 hours in order to avoid failure of the vessel. Before quenching experiments, the pressure was increased by ~30 bar to account for pressure loss upon cooling. The hot vessel was first air-cooled with compressed air until it stopped glowing and the pressure approximately decreased back to the run pressure (~60-90 s). The vessel was then dropped into a water-bath for the final quench. This complete process lasted 2 to 3 minutes, so a quench time of ~4 minutes is estimated.

2.2 Chemical analyses

After the removal of capsules from the vessel, they were dried and weighed to ensure that no weight loss or gain occurred during the experiment. Samples were embedded in epoxy, cut open along the center of the capsule, using a Buehler IsoMet precision saw, and polished for electron microprobe analysis. Upon polishing care was taken to ensure that the final sample surface was parallel to the long axis of the capsule, i.e., parallel to the diffusion direction.

All major element and halogen analyses were conducted with a JEOL JXA 8200 electron microprobe in the Department of Geoscience of the University of Mainz. Major elements were analyzed simultaneously with F and Cl using an acceleration voltage of 15 kV, a beam current of 12 nA, and a beam diameter of 10 μm. Dwell times of 120 and 30 s were used for F and Cl, respectively, and the detection limits for both were 60 ppm (1 σ). Dwell times of the major

184 elements were: Si 25s, Al 40s, Na 20s, K 30s, Ca 30s, Fe 60s, Mg 30s, Mn 50s and Ti 30s,
185 Standards used for calibration are SrF_2 (F), tugtupite (Cl, Na), VG-2 (Ca, Mg), VG-A99 (Fe, Si),
186 MnTi (Mn, Ti), and orthoclase (Al, K). VG-2, VG-A99, VG-568 and a natural obsidian standard
187 were analyzed repeatedly during each analytical session. The ZAF method was used for matrix
188 correction. As the crystal size was generally too small for quantitative EPMA analysis,
189 qualitative EDS maps of a small crystal-bearing area of sample 18X were acquired, being
190 representative of all crystal-bearing samples. The maps included F, Cl, and major elements (Ca,
191 Fe, Mg, Si, Al, Na, K) with a pixel size of 0.5 x 0.5 μm, using an acceleration voltage of 15 kV,
192 beam current of 30 nA, and dwell times of 280 ms for each element.
193 The transition from crystal-bearing to crystal-free glass was characterized by acquiring halogen
194 concentration profiles perpendicular to the diffusion interface. The F and Cl concentrations at the
195 interface (c_{liq}) were determined by calculating the average of the four points of the concentration
196 profile which are closest to the crystal interface (2 on each side). In 8 out of a total of 11
197 diffusion couple samples an additional line was measured for characterization of c_{liq}. In this
198 additional approach, a line parallel to the crystal-glass interface was first defined on a
199 backscattered image of the sample. Along this line, 20 - 25 spots per sample were measured with
200 fixed spacing (~80 – 100 μm) and from these spots the average concentrations of F and Cl were
201 calculated.
202

203 **2.3 Spectroscopic analyses**

204 To identify the microcrystalline silicate phases present in the experimental samples Raman
205 spectroscopy was carried out in the laboratories of the Department of Geoscience of the
206 University of Mainz, using a Horiba-Yvon Labram-HR Raman microscope with a focal length of

800 mm. A 200 mW diode-pumped solid-state laser with a wavelength of 532 nm was used as the excitation source. The spectra were recorded with a 50 x long-distance objective, and pinhole size and slit width of 400 µm and 100 µm, respectively, to ensure optimal confocal conditions. An edge filter was employed to suppress Rayleigh-scattering intensities. Spectra were collected within the interval from 200 to 1100 cm^{-1} as a single spectral window using a grating of 1800 grooves/mm. Due to the small crystal-size, recorded spectra usually contained some background signal related to the vibrational response of the glass matrix. Therefore, crystal-free areas in the experimental glasses were measured and compared to crystal-bearing measurements to identify the vibration bands of the crystalline phase. Spectra of crystals were then corrected by substracting the background and vibrational response of the glass matrix from the crystal-bearing signal.

To confirm homogeneity of H_2O within the experimental capsules, FTIR analyses were carried out on three representative samples (4X, 7X, and 15X), using a Thermo-Nicolet 6700 FTIR spectrometer coupled to a Continuum microscope at the JGU, Mainz. Doubly polished wafers with a thickness of ~120 – 220 µm were analyzed in transmission mode, covering the mid-IR and near-IR regions (450 – 6500 cm^{-1}) using a KBr beamsplitter and a MCT/A detector. Sample-free background spectra were collected every 20 minutes and each spectrum was acquired using a resolution of 4 cm^{-1} and 256 scans. Two samples (7X & 15X) were analyzed by line scans following the diffusion direction. Sample thickness was measured at at least 15 points per sample along the linear measurement traverses with a Mitutoyo precision micrometer. Thicknesses were then linearly interpolated to assign each analyzed spot with a corresponding thickness value. Single doubly polished glass fragments of sample 4X were analyzed by individual spot

measurements. Here, the sample thickness was determined by multiple measurements of each fragment. Bulk water content was determined from the height of the two absorbance peaks at 4500 cm^{-1} (OH) and 5200 cm^{-1} (H_2O_m) relative to a linear background below the peaks (e.g., Ihinger et al. 1994; Cherniak et al. 2010) and was calculated with Beer's law using the following extinction coefficients for trachyte: 1.58 l mol^{-1} and 1.36 l mol^{-1} (for the bands at 4500 cm^{-1} and 5200 cm^{-1} respectively; Di Matteo et al. 2004). Melt densities between 2446 – 2453 g l^{-1} were calculated using *DensityX* (Iacovino and Till 2019), which accounts for the average major element composition of the melt (Table 1) and the mass of water added to the glass during capsule preparation (Table 2).

Due to the presence of abundant crystals in some parts of the analyzed samples (Fig. 1), the measured water concentrations had to be corrected for the anhydrous crystal-content (e.g., von Aulock et al. 2014), which will "dilute" H_2O values by virtue of their occupying a fraction of the measurement path. Backscattered images of the respective samples were converted to binary images and analyzed for crystal-volume fraction using the software *ImageJ.* The water content in the crystal-bearing part was then corrected by the factor of crystal-abundance to achieve the final H_2O values.

3 Results

3.1 Starting glass compositions

The starting material compositions are provided in Table 1 and compared to bulk rock data of Castro et al. (2013). The data are based on the concentration profiles of the experimental

253 samples, measured by EPMA and were calculated from the average concentration of the 10
254 outermost points of each end of the concentration profiles (i.e., in areas that were unaffected by
255 diffusion and thus retained their pre-experimental major element and halogen concentration).
256 Where profiles of F or Cl did not exhibit a concentration plateau of sufficient length, less
257 analysis points were included in the calculation of F and Cl concentrations (min. 3 points).
258 Analyses with totals below 95 wt% or F and Cl values below 3 times the detection limit (180
259 ppm, 3 σ) were discarded. Analyses with elevated values of Fe, Mg and Ca co-occurring at the
260 same spot were interpreted to have been acquired on areas including crystals and were therefore
261 also discarded.
262
263 **3.2 Post-experimental sample textures**
264 All experiments (925 – 990 °C; 100 MPa; Table 2) produced glassy samples with only few small
265 bubbles (Fig. 1). In all but two experiments a single crystal phase developed. These euhedral
266 crystals range from <1 to a few 10s of μm in size and are of prismatic shape. They are chiefly
267 concentrated in spherulitic clusters, i.e., they form spheroidal aggregates of radially oriented
268 crystals (Fig. 1a) commonly associated with the process of devitrification (e.g., Keith and
269 Padden, 1963; Lofgren, 1971). The spherulites are up to 100 μm and they occur exclusively
270 scattered throughout the initially halogen-poor part of the sample. The border of the crystal-
271 bearing zone is well-defined and is approximately parallel to the initial diffusion couple
272 interface.
273 The two control experiments, 33X and 34X (both 950 °C), produced sample textures similar to
274 those observed within the spatial endmembers of the diffusion couples: the halogen-bearing melt
275 remained mostly crystal-free except for few anhedral crystal nuclei smaller than 1 μm (Fig. 1b).

The halogen-depleted sample developed spherulitic crystals throughout the whole charge (Fig. 1c). In one low-temperature experiment 26X (940 °C), the crystals did not form clusters throughout the entire halogen-poor zone. Instead, there are two textural transitions oriented roughly parallel to the diffusion front, one from glassy to crystal-bearing whereby with the crystals are randomly oriented and irregularly scattered, and a second transition from random to spherulitic aggregates (Fig. 1d). For the determination of c_{liq} (section 3.4) the transition to clustered crystal-bearing glass was analyzed. The zero-time experiment (7X) developed homogeneously distributed crystals in the halogen-poor half which are smaller in size but more numerous than those produced by the experiments of longer duration, and they show a very sharp transition to crystal-free glass at the initial diffusion interface (Fig. 1e).

The halogen-poor melt contains spherulitic crystals up to temperatures of at least 975°C at 100 MPa and is crystal-free at 990 °C. The halogen-enriched melt remains crystal-free down to temperatures of at least 940 °C but contains spherulites at 925 °C. The onset of crystallization in these experiments is interpreted to reflect that the melt was below the liquidus conditions. Considering 940 °C to be the lowest temperature at which halogen-bearing melt is crystal free (26X) and 990 °C to be the lowest temperature at which halogen-depleted melt is crystal free (22X), these results imply a liquidus depression of 50 °C for the highest measured values of c_{liq} (~0.51 wt% F, ~0.24 wt% Cl) in the melt of this study and at the experimental conditions (100 MPa, 3.5 – 4 wt% H_2O).

3.3 Glass and crystal chemistry

298 In the compositional map of sample 18X crystals show enrichment in Ca, Fe and Mg relative to
299 the melt (Fig. 2a – c, S1), suggesting clinopyroxene as was confirmed by Raman spectroscopy of
300 several grains in sample 24X. The Raman spectra showed two prominent peaks at ~664 and
301 ~1010 cm^{-1} and two smaller peaks at ~327 and ~392 cm^{-1}, respectively (Fig. 2d), consistent with
302 the three main vibration regions of clinopyroxene (Lafuente et al. 2015). The 1010 cm^{-1} peak is
303 ascribed to T-O stretching, while the peak at ~664 cm^{-1} is caused by chain bending/stretching
304 modes. The two low-frequency bands in the region 400 cm^{-1} are characteristic of the vibrational
305 response of both M-sites (e.g., Tribaudino et al. 2012). The broad double band between 700 and
306 800 cm^{-1} is a remnant signal of the glass matrix (e.g., Helo et al., 2020). The slight depletion of
307 Mg and Ca in the glass of CC2 (Table 1) agrees well with the presence of clinopyroxene crystals
308 and the corresponding depletion of these elements in the melt.
309
310 All concentration profiles exhibit typical diffusion patterns of F and Cl (e.g., Feisel et al. 2019)
311 while the major element concentrations are relatively constant (Fig. 3). Some variability along
312 the profile is observed in SiO_2 content, possibly related to the presence of microlites on the
313 crystal-bearing, halogen-poor side and concomitant shift in residual glass composition due to the
314 growth of crystals. Furthermore, on the crystal bearing side of the diffusion couple scatter of
315 FeO, MgO and CaO concentrations is likely caused by analyses partly covering crystals. This
316 effect is particularly pronounced in the zero-time experiment 7X, which contains abundant small
317 crystals which could not be avoided during data acquisition. Most analyses yielded totals
318 between 96 and 97 wt%, which is consistent with the expected H_2O-concentration in the capsule.
319

FTIR analyses on 3 representative samples showed mostly homogeneous distribution of H_2O with variation limited to just a few tenths of weight percent. However, due to the lack of appropriate published extinction coefficients for the melt composition used in our study, and the presence of abundant crystals, the absolute values determined by FTIR are considered to be only approximate. For example, in sample 15X a water concentration of 4.2 wt% was determined for both, the crystal-bearing and crystal-absent parts of the sample. However, upon preparation of the sample, only 3.67 wt% of H_2O was added (Table 2). This water content (3.67 wt%) is considered to be a maximum possible value as a small loss of water during the subsequent preparation of the capsule (tamping, welding etc.) could have occurred. Water-gain, in contrast, is not likely to have occurred during the experiment, and was monitored for by weighing the capsule directly before and after the experiment. The overestimation of the water content in sample 15X is therefore likely a consequence of the presence of bubbles in parts of the sample and the lack of appropriate extinction coefficients for the melt composition used. Sample 4X has an average water content of 3.4 and 3.5 wt% in the crystal-bearing and crystal-free parts, respectively. The crystal-content of this sample is similar to that of 15X (6% compared to 4%). The zero-time experiment 7X also shows a homogeneous H_2O-profile with 3.7 and 3.9 wt% in the crystal-free and -bearing parts, respectively. The water content in this sample was corrected considering a crystal-content of 15% in the crystal-bearing part. The data of all measured FTIR profiles are provided in the supplementary material (Fig. S2).

3.4 Assessment of "c_{liq}": F and Cl concentration at the transition from crystal-free to -bearing glass

342 A section of a typical concentration profile is shown in Figure 3. In these diagrams, the transition
343 to crystal-bearing glass (dashed orange line) is displaced with respect to the original interface
344 between the diffusion-couple halves (dashed white line). Figure 3b shows a backscattered image
345 spatially coincident to the concentration profile geometries of sample 4X. This image shows that
346 the transition from crystal-free melt (bottom) to crystal-bearing melt (top) is indeed quite sharp.
347 Figure 3c shows the corresponding homogeneous major element concentrations. The c_{liq} data of
348 F and Cl is presented in Table 2 and illustrated in Figure 4. c_{liq} values are in the range of 0.19 –
349 0.52 and 0.07 – 0.24 wt%, respectively with higher values corresponding to lower experimental
350 temperatures. In Table 2, the data labelled "profile" is based on the diffusion profile approach
351 and data labelled "diss. front" is based on analyses along the transition interface. Values
352 determined by the two different methods agree well for each sample. All concentration vs.
353 distance diagrams for F, Cl and all major elements, measured along the diffusion direction and
354 the dissolution front are provided in the supplementary material (Fig. S3 & S4).
355
356
357 # 4 Discussion
358
359 ## 4.1 Assessment of experimental approach
360 In this study, the influence of F and Cl on a near-liquidus silicic melt (Castro et al. 2013) has
361 been determined using a dynamic disequilibrium approach. The diffusion couple technique
362 imposes a large concentration range of F and Cl in a single experiment and permits investigation
363 of the whole range of compositions – from the extreme initial values to every intermediate
364 concentration – at constant *P-T* conditions. This of course assumes that the diffusion of halogens

365 at these conditions is slow enough to facilitate a response of the melt (e.g., crystal dissolution) on
366 a local scale (tens of μm). Even though no equilibrium state can be reached during the short
367 timescale of diffusion experiments, the melt does, however, react to the changing halogen
368 concentrations in the form of crystal dissolution. The quenched glass can therefore be used as a
369 series of chemical and textural "snapshots" of the systems's approach to equilibrium, including a
370 robust record of varying halogen concentrations. Key to this approach is to bring the diffusion
371 couple to a near-liquidus temperature (with respect to the halogen-poor melt). At these *T*-
372 conditions, the halogen-rich melt is well above its liquidus. While the duration of equilibrium
373 experiments is required to be sufficiently large to achieve equilibrium (e.g., Pichavant et al.
374 2007), our experiments were deliberately quenched quickly enough so as to preserve the
375 diffusion concentration profiles which span the full range of F and Cl concentrations.
376
377 **Diffusion profile fitting.** The concentration profiles (e.g., Castro et al. 2008; Zhang 2010), were
378 fitted with the equation representing constant one-dimensional diffusivity between two semi-
379 infinite media in a Cartesian coordinates (Crank 1975):

$$c(x,t) = \frac{c_{low} + c_{high}}{2} + \frac{c_{low} - c_{high}}{2} * \mathrm{erf}\left(\frac{x - x_0}{2 * \sqrt{Dt}}\right) \qquad (1)$$

380 where *c(x,t)* is the concentration (wt%) at distance *x* (m) after the experimental time *t* (s). c_{low} and
381 c_{high} (wt%) are the initial concentrations of each half-space, x_0 (m) the position of the diffusion
382 interface which is only used for fitting purposes (Zhang 2010). *D* (m^2/s) is the diffusion
383 coefficient. One example of a fitted concentration profile (15X) is shown in Figure 5. The good
384 correlation between the concentration profile and the solution to the diffusion equation (1) shows
385 that melt crystallization does not affect halogen diffusion, i.e., that the halogens are diffusing
386 independently and are in turn affecting the crystallization of the melt.

387

388 **Progression of crystal-growth and dissolution.** The zero-time experiment revealed that
389 spherulitic clinopyroxene grew in the halogen-poor half within the heating phase of ~45 min
390 (Fig. 1e), indicating that crystal growth was initiated before any substantial flux of halogen
391 diffusion had occurred. A sharp transition developed from crystal-free to crystal-bearing glass
392 and crystals grew with the same spherulitic morphology as in the longer experiments. Given
393 these observations, we infer that 1) all diffusion couples began with a textural configuration of a
394 crystal-free, halogen-rich melt juxtaposed against a crystal-free, halogen-poor melt, 2) crystal-
395 free, halogen-poor melt experienced crystallization during the heating phase and thus in the
396 absence of any substantial diffused halogen contribution to the melt, whereas the halogen
397 contents of the halogen-rich melt inhibited such crystallization, and 3) diffusion of halogens into
398 the crystal-bearing zone during the subsequent experimental run, causing crystal dissolution
399 whose progress describes a planar dissolution front.

400

401 A glass transition temperature of ~350 °C was calculated based on the halogen-poor composition
402 CC2 (Table 1) using the method of Giordano et al. (2008) and considering an average water
403 concentration of 3.7 wt%. The spherulites present here, comprising individual crystals that are
404 not in direct contact with each other, could have formed by devitrification at relatively low
405 degrees of undercooling and above T_g (Fenn 1977; Lofgren 1980; McArthur et al. 1998). The
406 ensuing process of crystal dissolution during advancement of the halogen diffusion front at
407 isothermal conditions rules out kinetic effects that may be introduced by heating or cooling. This
408 ensures that no activation energy associated with crystal nucleation must be overcome, as would
409 be the case in a crystallization scenario (e.g., Kirkpatrick 1983; Burkhard 2005). The latter would

result in a "delayed" response of the melt to the changing halogen concentrations leading to biased readings of c_{liq}. We therefore consider the measured halogen concentrations at the dissolution front to represent the halogen concentrations of the liquidus composition, which is defined by the halogen concentration necessary to keep the melt crystal-free at the experimental *P-T* conditions. The significance of the measured liquidus composition is further confirmed by the two control experiments 33X and 34X which developed similar textures like the diffusion couples and verified the liquidus depressing effect even over the longer run duration of ~30 hours.

Br and I in the melt. As the initial halogen-bearing starting glass CC1 was also enriched in Br and I, their potential effect on crystal dissolution needs to be assessed. The diffusivity of Br was shown to be almost one order of magnitude slower than Cl in hydrous phonolitic melt (Balcone-Boissard et al. 2020) at 1250 – 1450 °C and in dry rhyodacitic melt (Feisel et al. 2021) at 850 – 1100 °C . However, our own unpublished data indicates Br diffusivity in the hydrous melt used in this study may be only slightly slower than Cl (<< 1 log unit). Even though the effect of Br on the phase equilibria cannot be completely ruled out, Br is not known to preferably bond with the major elements of clinopyroxene but has instead been demonstrated to form complexes with Na (Cochain et al. 2015; Webster et al. 2018). Therefore, we consider the effect of Br on clinopyroxene dissolution in our study to be negligible.

The diffusivity of I was found to be substantially slower than Br in dry rhyodacite and also in the hydrous trachytic melt used in the present study. We therefore conclude that on the timescales of the current experiments I mobility will be insignificant, and its concentration distribution will not deviate from the initial concentration geometry in the diffusion couple. Consequently, the

433 crystal-dissolution front is not expected to correlate with I concentrations and thus, we consider
434 that I has no effect on melt crystallization or resorption.
435
436 **Comparison to equilibrium experiments.** Our experimental approach was further assessed by
437 comparison to a phase-equilibrium study on a very similar melt composition. Castro et al. (2013)
438 experimentally reproduced the mineral and glass compositions observed in the 2011 Cordón
439 Caulle rhyolite magma to infer pre-eruptive magma storage and ascent conditions. They used
440 natural pumiceous samples of the Plinian phase of the eruption, with a major element
441 composition almost identical to that of the obsidian lava used as base material for the present
442 experiments (Table 1). They applied a very similar experimental setup (NNO +1) and their
443 starting material contained 0.14 – 0.2 wt% Cl which is comparable to the halogen-enriched
444 starting composition of our study. No data on F concentration is available from their study,
445 however, Schipper et al. (2019) report F concentrations around 0.1 wt% in the matrix glass of
446 pyroclasts of the same eruption.
447 Castro et al. (2013) found the liquidus temperature to be in the range of 940 – 950 °C, at a
448 pressure of 100 MPa with ilmenite and magnetite being on the liquidus at these conditions.
449 Clinopyroxene appeared in the phase assemblage about 40 °C lower. In our experiments, the
450 liquidus temperature of halogen-enriched melt is similar to but at the lower end of this range
451 (~950 – 900 °C) and is defined by the appearance of clinopyroxene. This offset is likely a
452 consequence of slight compositional differences between the melts, particularly the enhanced Na
453 and F contents transferred to the melt via sodium-salts during sample synthesis (Table 1).
454 Additionally, while the experiments performed by Castro et al. (2013) were saturated in H_2O,
455 those of this study were, by design, slightly undersaturated at 100 MPa (3.5 – 4 wt% H_2O) in

456 order to avoid formation of gas bubbles. The correspondingly lower water activity in our
457 experiments at equivalent confining pressure (100 MPa) explains some observed difference in
458 liquidus relations between our and Castro et al.'s study (e.g., see also Scaillet et al. 2016).
459
460 **4.2 Effects of F and Cl on the melt liquidus temperature**
461 The halogen concentrations necessary to suppress crystallization at a given temperature (c_{liq})
462 were quantified (Table 2). All experiments which resulted in a partially crystal-bearing sample
463 can be viewed as experiments whose halogen concentrations at the dissolution front essentially
464 define the liquidus composition at that temperature. c_{liq} decreases linearly with increasing
465 temperature (Fig. 4a) which shows that the depression of the liquidus temperature is proportional
466 to the halogen contents. This trend is illustrated in Figure 4b which shows the relation between
467 the concentration of F and Cl and the liquidus depression (ΔT). The liquidus depression
468 represents the difference between the liquidus temperature of halogen-poor melt at ~990 °C
469 (22X) and the run temperatures of each plotted experiment.
470
471 Fig. 4b indicates that Cl is about twice as effective as F in depressing the liquidus. Indeed,
472 considering their molar masses, Cl is almost 4 times more effective per atom than F. However,
473 the concentrations of F and Cl measured at the dissolution front cannot be viewed as independent
474 variables, as they each diffuse with a constant diffusivity over the same time period and at the
475 same *P*-*T* conditions. So the ratio of their concentrations will be dictated by their diffusivities
476 and run time. In summary, even though ΔT increases more strongly with increasing Cl than F, it
477 is not possible to attribute the liquidus depressing effect to one of the halogens based on the
478 values of c_{liq}.

Insights into the potential effects of the individual halogens may be elucidated by their typical bonding behavior. Previous studies have shown that F complexes with Al in aluminosilicate melts (Kohn et al. 1991; Schaller et al. 1992; Kiprianov and Karpukhina 2006; Karpukhina et al. 2007), but may also form species with Na, Mg or Ca (Zeng and Stebbins 2000; Kiczenski et al. 2004; Mysen et al. 2004). Additionally, pronounced fluorine complexation of Mg over Fe was shown for a Mg – Fe rich basalt (Filiberto et al. 2014) and other studies found evidence for Si – F bonding in silicate melts (e.g., Liu and Nekvasil 2002). In particular the strong association of the network modifying cations Mg and Ca with F indicates that F has the potential to bond with two major components of clinopyroxene.

Cl was also shown to commonly bond with network modifying cations such as Ca and Mg, and especially Fe (e.g., Dingwell and Hess 1998; Webster and De Vivo 2002; Filiberto and Treiman 2009; Dolejš and Zajacz 2018). Along with the study of Bell and Webster (2015), who showed that the presence of Cl increases Fe solubility and affects the availability of Fe for magnetite crystallization in hydrous rhyodacitic melts, our results show a similar effect for clinopyroxene. According to Webster and De Vivo (2002) the solubility of Cl in a melt increases with the abundances of $Mg \approx Ca > Fe^{2+} >> Na > K$. This indicates that dissolved Cl preferably bonds with the major components of clinopyroxene crystals Ca, Mg and Fe. As both halogens likely have the potential to complex with some of the main components of clinopyroxene, namely F with Mg and Ca, and Cl with Mg, Ca and Fe, we propose that crystal dissolution is a consequence of both halogens diffusing into the crystal-bearing melt. The presence of F and Cl enhances the solubility and reduces the activity of CaO, MgO and FeO for clinopyroxene crystallization.

This is the peer-reviewed, final accepted version for American Mineralogist, published by the Mineralogical Society of America.
The published version is subject to change. Cite as Authors (Year) Title. American Mineralogist, in press.
DOI: https://doi.org/10.2138/am-2022-8120. http://www.minsocam.org/

As no major element analyses of clinopyroxene are available, it is not possible to quantitatively compare crystals grown in halogen-bearing and halogen-depleted melt (e.g., 17X) to determine which of the constituents of clinopyroxene is the most affected by dissolved halogens. The weak depletion of CaO and MgO in the averaged bulk composition of the halogen-depleted melt (CC2; Table 1) indicates that the clinopyroxene may be composed of mainly these two components and only to a minor extent of FeO. This in turn argues that mainly Mg – or Ca – complexes should be formed by crystal dissolution which can be attributed to both, F – and Cl – interaction.

Quantification of the liquidus depression. In order to quantify the liquidus depression as a function of halogen concentration, all F and Cl atoms are considered to be equally involved in the dissolution process. Even though this assumption is likely not representative of the actual experimental processes, it does, however, allow us to constrain a relation between halogen concentration and liquidus depression. The concentrations of F and Cl were first recalculated to mol% and summed to plot the data relative to ΔT (Fig. 6). The data can be described using the following regression:

$$\Delta T = 1575 \pm 379 \left(\frac{K}{mol\%}\right) * c\ (mol\%) - 8.894 \qquad (2)$$

Where c is the sum of the concentrations of F and Cl. The uncertainty of the linear regression represents the 95 % confidence interval (2 σ).

Equation (2) gives the minimum depression of the liquidus assuming that both halogens are equally involved. If only one of the halogens was responsible for the crystal dissolution, the regression line would follow the respective data points of F or Cl and likewise increase in slope

(Fig. 6). For example, if crystal dissolution was caused by Cl alone, the datapoints of F would not contribute to the regression and the slope would be 6902 ± 1763 (K/mol% Cl), which means a ~4 times stronger effect than by combined halogens. This is the maximum liquidus depression that can be inferred from the present data. However, as discussed above, only the minimum depression of the liquidus (eq. 2) is considered reliable due to the limitations of this dataset in determining the individual effects of F and Cl.

The quantification of the liquidus depression (eq. 2) is only valid at the H_2O concentrations and range of F- and Cl-concentrations investigated here. The concentration range is bracketed by the first appearance of crystals in the halogen-enriched melt (~0.87 wt% F, ~0.36 wt% Cl) to the point where no crystals are observed in the halogen-poor melt (~0.04 wt% F, ~0.06 wt% Cl). The relation may be valid for even lower temperatures, under the condition that halogen concentrations would be further enriched beyond the values studied in the investigated melts (e.g., Filiberto and Treiman 2009).

As most recent studies on the liquidus depression effect of halogens were carried out on basaltic melt involving either F or Cl (e.g., Filiberto et al. 2012, 2014), a direct comparison to the present study is not straightforward. Nevertheless, the equations provided by Filiberto et al. 2012, 2014 and Farcy et al. 2016 were applied. The highest c_{liq} concentrations observed in the present study are 0.52 wt% F and 0.23 wt% Cl (940 °C; 26X), which together yield a total halogen content of 0.034 mol% in the melt (Table 2). Based on this total halogen content, equivalent concentrations of F and Cl were calculated, assuming that in each case the total halogen content (0.034 mol%) was given by either F or Cl only. Accordingly, the resultant equivalent F and Cl concentrations

545 (~0.6 wt% and ~1.2 wt% respectively) yield ΔT values of ~34 K for F-enrichment (Filiberto et
546 al. 2012) and ~16 K for Cl-enrichment (Filiberto et al. 2014; Farcy et al. 2016) in basaltic melt.
547 For the melt of the present study, the calculated ΔT is ~45 K, which is ~1.3 and ~2.8 times more
548 effective than the effects observed for F and Cl in basalt, respectively.
549
550 **Implications for magmatic processes.** The liquidus-depressing effect of the halogens has
551 implications for several magmatic scenarios and may also affect other alkaline earth element and
552 Fe-bearing crystals as was shown in related studies for olivine and pyroxene in basalt causing a
553 liquidus depression of up to 50 °C (Filiberto et al. 2012, 2014). Increased abundance of F or Cl
554 may promote enhanced magma production in addition to that controlled by dissolved H_2O only.
555 Furthermore, we suggest that F and Cl may have the potential to hinder crystallization of a near-
556 liquidus degassing magma. The halogens could depress the liquidus beyond the temperature
557 implied by H_2O alone and keep the magma crystal-free even though H_2O may already have been
558 degassed. Especially F but also Cl has been shown to remain dissolved in the melt until relatively
559 shallow crustal levels (e.g., Spilliaert et al. 2006; Schipper et al. 2019) and could therefore
560 promote crystal-free melt even after loss of H_2O.
561
562 An example for a natural analogue to the present experimental conditions (constant P, T and H_2O
563 content) would be a slowly cooling dome or lava flow such as the obsidian flow of the 2011
564 Cordón Caulle eruption. Schipper et al. (2019) studied the petrological and chemical properties
565 of lavas and tephra of this eruption and found that natural lava samples with high amounts of
566 microlites (> 75%) have drastically lower matrix glass F and Cl concentrations than those with
567 lower microlite-content (< 75%). The halogen concentration in these lava samples was reported

568 to be more similar to contents measured in plagioclase- or pyroxene-hosted melt inclusions
569 (Schipper et al. 2019), representative of an earlier stage of magma differentiation. They
570 concluded that crystallization caused halogens to leave the melt in a process analogous to second
571 boiling. Our results indicate that the process of halogen diffusion and ensuing crystallization may
572 appear reversed in nature, involving crystallization *in response* to halogen devolatilization.
573 This shows that halogens can have a large influence on melt crystallinity even at constant
574 temperatures and at potentially various scenarios. Thus, halogen devolatilization may be one
575 controlling factor for the bulk rheological characteristics of a magmatic body or a lava flow by
576 enhancing microlite crystallization.
577
578
579 **5 Implications**
580
581 The effects of halogen concentration on the crystallinity of a near-liquidus hydrous trachytic melt
582 were studied experimentally with a disequilibrium approach by applying the diffusion couple
583 technique. The influence of F and Cl on the dissolution of spherulitic clinopyroxene was
584 pronounced in all experiments, and we interpret this to manifest depression of the hydrous melt
585 liquidus by about 50 °C. The halogen-poor melt crystallized spherulitic clinopyroxene during
586 heating, whereas no crystallization occurred in the halogen-enriched melt. The minimum effect
587 of the halogens on the depression of the liquidus in the studied melt was quantified and is shown
588 to be ~2.8 times more pronounced than in basalt enriched with an equivalent amount of Cl.
589

590 The disequilibrium technique can potentially be used to investigate the influence of minor yet
591 influential chemical components on the phase equilibria by providing "snapshots" of the system
592 approaching equilibrium. Diffusion couple experiments are well suited for this technique as they
593 allow to track the influence of one or few components, covering the full concentration range
594 between the two starting compositions. This approach is, however, limited to systems where the
595 crystal dissolution or crystallization occurs on a shorter timescale than the diffusion of the
596 respective chemical components. We suggest this technique to be particularly suited to
597 complement conventional *P*-*T*-*x* experiments, e.g., to investigate intermediate steps of *x* (e.g.,
598 H_2O, halogens etc.) at fixed *P*-*T* conditions. Additionally, applying this technique as a standalone
599 approach was shown to be useful in describing the response of a melt with a dynamically
600 changing chemical composition, which is for example comparable to the process of
601 devolatilization of a melt or lava.
602
603 The results of this study illustrate the influence of halogens on the stability of near-liquidus
604 silicates in a temperature range applicable to silicic lava flows and domes. We demonstrate that
605 even a small concentration enhancement of few hundreds of ppms of halogens in a melt of
606 otherwise fixed H_2O-content can affect the stability of Ca-Fe-Mg mineral phases. As crystal-
607 content is one of the most influential physical factors governing magma rheology (e.g., Maron
608 and Pierce 1956; Mueller et al. 2010; Klein et al. 2017), our results have implications for how
609 magmas evolve physically and chemically during their ascent in the conduit and whether they
610 erupt explosively or effusively.
611
612 **Acknowledgements**

We appreciate the help of B. Scheu, U. Kueppers and K.-U. Hess with sample preparation and thank N. Groschopf, S. Buhre and T. Haeger for their assistance with electron microprobe and Raman analyses.

This research is part of the Ph.D. thesis of Y. Feisel and is supported by a fellowship of the Gutenberg Research College of the Johannes Gutenberg-University of Mainz to D.B. Dingwell. D.B. Dingwell acknowledges the support of ERC 2018 ADV Grant 834225 (EAVESDROP). Part of this research was performed within the infrastructure established by the VAMOS research center of the Johannes Gutenberg-University, Mainz.

The authors thank J. Filiberto and two anonymous reviewers for their perceptive reviews and A. Cadoux for the editorial handling of this manuscript.

References

Aiuppa, A., Baker, D.R., and Webster, J.D. (2009) Halogens in volcanic systems. Chemical Geology, 263, 1–18.

Alloway, B. V., Pearce, N.J.G., Villarosa, G., Outes, V., and Moreno, P.I. (2015) Multiple melt bodies fed the AD 2011 eruption of Puyehue-Cordón Caulle, Chile. Scientific Reports, 5, 1–8.

Balcone-Boissard, H., Baker, D.R., Villemant, B., Cauzid, J., Boudon, G., and Deloule, E. (2020) Br diffusion in phonolitic melts: Comparison with fluorine and chlorine diffusion. American Mineralogist, 105, 1639–1646.

Bell, A.S., and Simon, A. (2011) Experimental evidence for the alteration of the $Fe^{3+}/\Sigma Fe$ of silicate melt caused by the degassing of chlorine-bearing aqueous volatiles. Geology, 39, 499–502.

Bell, A.S., and Webster, J.D. (2015) Dissolved Cl, oxygen fugacity, and their effects on Fe

behavior in a hydrous rhyodacitic melt. American Mineralogist, 100, 1595–1599.

Brey, G.P., Bulatov, V.K., and Girnis, A. V. (2009) Influence of water and fluorine on melting of carbonated peridotite at 6 and 10 GPa. Lithos, 112, 249–259.

Burkhard, D.J.M. (2005) Nucleation and growth rates of pyroxene, plagioclase, and Fe-Ti oxides in basalt under atmospheric conditions. European Journal of Mineralogy, 17, 675–686.

Carroll, M.R., and Webster, J.D. (1994) Solubilities of sulfur, noble gases, nitrogen, chlorine, and fluorine in magmas. In M.R. Carroll and J.R. Holloway, Eds., Volatiles in Magmas Vol. 30, pp. 231–279. Rev. Mineral.

Castro, J.M., Beck, P., Tuffen, H., Nichols, A.R.L., Dingwell, D.B., and Martin, M.C. (2008) Timescales of spherulite crystallization in obsidian inferred from water concentration profiles. American Mineralogist, 93, 1816–1822.

Castro, J.M., Schipper, C.I., Mueller, S.P., Militzer, A.S., Amigo, A., Parejas, C.S., and Jacob, D. (2013) Storage and eruption of near-liquidus rhyolite magma at Cordón Caulle, Chile. Bulletin of Volcanology, 75, 1–17.

Castro, J.M., Cordonnier, B., Schipper, C.I., Tuffen, H., Baumann, T.S., and Feisel, Y. (2016) Rapid laccolith intrusion driven by explosive volcanic eruption. Nature Communications, 7, 13585.

Cherniak, D.J., Hervig, R., Koepke, J., Zhang, Y., and Zhao, D. (2010) Analytical methods in diffusion studies. Reviews in Mineralogy and Geochemistry, 72, 107–170.

Chevychelov, V.Y., Botcharnikov, R.E., and Holtz, F. (2008) Partitioning of Cl and F between fluid and hydrous phonolitic melt of Mt. Vesuvius at ~ 850-1000 °C and 200 MPa. Chemical Geology, 256, 172–184.

Clarke, D.B., Wunder, B., Förster, H.-J., Rhede, D., and Hahn, A. (2009) Experimental investigation of near-liquidus andalusite-topaz relations in synthetic peraluminous haplogranites at 200 MPa. Mineralogical Magazine, 73, 997–1007.

Cochain, B., Sanloup, C., de Grouchy, C., Crépisson, C., Bureau, H., Leroy, C., Kantor, I., and Irifune, T. (2015) Bromine speciation in hydrous silicate melts at high pressure. Chemical Geology, 404, 18–26.

Crank, J. (1975) The Mathematics of Diffusion. Clarendon-Oxford, London.

Di Matteo, V., Carroll, M.R., Behrens, H., Vetere, F., and Brooker, R.A. (2004) Water solubility in trachytic melts. Chemical Geology, 213, 187–196.

671 Dingwell, D.B., and Hess, K.U. (1998) Melt viscosities in the system Na-Fe-Si-O-F-Cl;
672 contrasting effects of F and Cl in alkaline melts. American Mineralogist, 83, 1016–1021.
673 Dingwell, D.B., Scarfe, C.M., and Cronin, D.J. (1985) The effect of fluorine on viscosities in the
674 system Na2O - Al2O3 - SiO2: implications for phonolites, trachytes and rhyolites.
675 American Mineralogist, 70, 80–87.
676 Dolejš, D., and Baker, D.R. (2007a) Liquidus equilibria in the system K_2O-Na_2O-$A1_2O_3$-SiO_2-
677 F_2O_{-1}-H_2O to 100 MPa: I. Silicate-fluoride liquid immiscibility in anhydrous systems.
678 Journal of Petrology, 48, 785–806.
679 ——— (2007b) Liquidus equilibria in the system K_2O-Na_2O-Al_2O_3-SiO_2-F_2O_{-1}-H_2O to 100
680 MPa: II. Differentiation paths of fluorosilicic magmas in hydrous systems. Journal of
681 Petrology, 48, 807–828.
682 Dolejš, D., and Zajacz, Z. (2018) Halogens in Silicic Magmas and Their Hydrothermal Systems.
683 In D.E. Harlov and L.Y. Aranovich, Eds., The Role of Halogens in Terrestrial and
684 Extraterrestrial Geochemical Processes pp. 431–543. Springer-Verlag, Cham.
685 Evans, K.A., Mavrogenes, J.A., O'Neill, H.S., Keller, N.S., and Jang, L.Y. (2008) A preliminary
686 investigation of chlorine XANES in silicate glasses. Geochemistry, Geophysics,
687 Geosystems, 9, 1–15.
688 Farcy, B.J., Gross, J., Carpenter, P., Hicks, J., and Filiberto, J. (2016) Effect of chlorine on near-
689 liquidus crystallization of olivine-phyric shergottite NWA 6234 at 1 GPa: Implication for
690 volatile-induced melting of the Martian mantle. Meteoritics and Planetary Science, 51,
691 2011–2022.
692 Feisel, Y., Castro, J.M., and Dingwell, D.B. (2019) Diffusion of F and Cl in dry rhyodacitic melt.
693 American Mineralogist, 104, 1689–1699.
694 Feisel, Y., Castro, J.M., Helo, C., and Dingwell, D.B. (2021) Halogen diffusion in silicic melts.
695 In EMPG - XVII 17th International Symposium on Experimental Mineralogy, Petrology
696 and Geochemistry: Abstract Volume p. 110. Potsdam.
697 Fenn, P.M. (1977) The nucleation and growth of alkali feldspars from hydrous melts. The
698 Canadian Mineralogist, 15, 135–161.
699 Filiberto, J., and Treiman, A.H. (2009) The effect of chlorine on the liquidus of basalt: First
700 results and implications for basalt genesis on Mars and Earth. Chemical Geology, 263, 60–
701 68.

Filiberto, J., Wood, J., Dasgupta, R., Shimizu, N., Le, L., and Treiman, A.H. (2012) Effect of fluorine on near-liquidus phase equilibria of an Fe-Mg rich basalt. Chemical Geology, 312–313, 118–126.

Filiberto, J., Dasgupta, R., Gross, J., and Treiman, A.H. (2014) Effect of chlorine on near-liquidus phase equilibria of an Fe-Mg-rich tholeiitic basalt. Contributions to Mineralogy and Petrology, 168, 1–13.

Foley, S.F., Taylor, W.R., and Green, D.H. (1986a) The effect of fluorine on phase relationships in the system $KAlSiO_4$-Mg_2SiO_4-SiO_2 at 28 kbar and the solution mechanism of fluorine in silicate melts. Contributions to Mineralogy and Petrology, 93, 46–55.

——— (1986b) The role of fluorine and oxygen fugacity in the genesis of the ultrapotassic rocks. Contributions to Mineralogy and Petrology, 94, 183–192.

Geschwind, C.H., and Rutherford, M.J. (1995) Crystallization of microlites during magma ascent: the fluid mechanics of 1980-1986 eruptions at Mount St Helens. Bulletin of Volcanology, 57, 356–370.

Giordano, D., Russell, J.K., and Dingwell, D.B. (2008) Viscosity of magmatic liquids: A model. Earth and Planetary Science Letters, 271, 123–134.

Gonnermann, H.M., and Manga, M. (2007) The fluid mechanics inside a volcano. Annual Review of Fluid Mechanics, 39, 321–356.

Helo, C., Castro, J.M., Hess, K.U., and Dingwell, D.B. (2020) Determination of water speciation in hydrous haplogranitic glasses with partial Raman spectra. Chemical Geology, 553, 119793.

Hirayama, C., and Camp, E. (1969) The effect of fluorine and chlorine substitution on the viscosity and fining of soda-lime and potassium-barium silicate glass. Glass Technology, 10, 123.

Iacovino, K., and Till, C.B. (2019) DensityX: A program for calculating the densities of magmatic liquids up to 1,627 °C and 30 kbar. Volcanica, 2, 1–10.

Ihinger, P.D., Hervig, R.L., and McMillan, P.F. (1994) Analytical methods for volatiles in glasses. In M.R. Carroll and J.R. Holloway, Eds., Volatiles in Magmas Vol. 30, pp. 67–121. Rev. Mineral., Mineralogical Society of America, Washington, D.C.

Karpukhina, N.G., Werner-Zwanziger, U., Zwanziger, J.W., and Kiprianov, A.A. (2007) Preferential binding of fluorine to aluminum in high peralkaline aluminosilicate glasses.

733 Journal of Physical Chemistry B, 111, 10413–10420.
734 Keith, H.D., and Padden, F.J. (1963) A phenomenological theory of spherulite crystallization.
735 Journal of Applied Physics, 34, 2409–2421.
736 Kiczenski, T.J., Du, L.S., and Stebbins, J.F. (2004) F-19 NMR study of the ordering of high field
737 strength cations at fluoride sites in silicate and aluminosilicate glasses. Journal of Non-
738 Crystalline Solids, 337, 142–149.
739 Kiprianov, A.A., and Karpukhina, N.G. (2006) Oxyhalide silicate glasses. Glass Physics and
740 Chemistry, 32, 1–27.
741 Kirkpatrick, R.J. (1983) Theory of nucleation in silicate melts. American Mineralogist, 68, 66–
742 77.
743 Klein, J., Mueller, S.P., and Castro, J.M. (2017) The influence of crystal size distributions on the
744 rheology of magmas: New insights from analog experiments. Geochemistry, Geophysics,
745 Geosystems, 18, 4055–4073.
746 Kohn, S.C., Dupree, R., Mortuza, M.G., and Henderson, C.M.B. (1991) NMR evidence for five-
747 and six-coordinated aluminum fluoride complexes in F-bearing aluminosilicate glasses.
748 American Mineralogist, 76, 309–312.
749 Koster van Groos, A.F., and Wyllie, P.J. (1968) Melting relationships in the system $NaAlSi_3O_8$-
750 NaF-H_2O to 4 kilobars pressure. Journal of Geology, 76, 50–70.
751 ——— (1969) Melting relationships in the system $NaAlSi_3O_8$-NaCl-H_2O at one kilobar pressure,
752 with petrological applications. Journal of Geology, 77, 581–605.
753 Lafuente, B., Downs, R.T., Yang, H., and Stone, N. (2015) The power of databases: The RRUFF
754 project. In T. Armbruster and R.M. Danisi, Eds., Highlights in Mineralogical
755 Crystallography pp. 1–29. De Gruyter, Berlin.
756 Liu, Y., and Nekvasil, H. (2002) Si-F bonding in aluminosilicate glasses: Inferences from ab
757 initio NMR calculations. American Mineralogist, 87, 339–346.
758 Lofgren, G. (1971) Spherulitic textures in glassy and crystalline rocks. Journal of Geophysical
759 Research, 76, 5635–5648.
760 ——— (1980) Experimental Studies on the Dynamic Crystallization of Silicate Melts. In R.B.
761 Hargraves, Ed., Physics of Magmatic Processes pp. 487–551. Princeton University Press,
762 Princeton, New Jersey.
763 Manning, D.A.C. (1981) The effect of fluorine on liquidus phase relationships in the system Qz-

764 Ab-Or with excess water at 1 kB. Contributions to Mineralogy and Petrology, 76, 206–215.
765 Maron, S.H., and Pierce, P.E. (1956) Application of Ree-Eyring generalized flow theory to
766 suspension of spherical particles. Journal of Colloid Science, 11, 80–95.
767 Matthews, W., Linnen, R.L., and Guo, Q. (2003) A filler-rod technique for controlling redox
768 conditions in cold-seal pressure vessels. American Mineralogist, 88, 701–707.
769 McArthur, A.N., Cas, R.A.F., and Orton, G.J. (1998) Distribution and significance of crystalline,
770 perlitic and vesicular textures in the Ordovician Garth Tuff (Wales). Bulletin of
771 Volcanology, 60, 260–285.
772 Mueller, S., Llewellin, E.W., and Mader, H.M. (2010) The rheology of suspensions of solid
773 particles. In Proceedings of the Royal Society A pp. 1201–1228.
774 Mysen, B.O., Cody, G.D., and Smith, A. (2004) Solubility mechanisms of fluorine in peralkaline
775 and meta-aluminous silicate glasses and in melts to magmatic temperatures. Geochimica et
776 Cosmochimica Acta, 68, 2745–2769.
777 Pichavant, M., Costa, F., Burgisser, A., Scaillet, B., Martel, C., and Poussineau, S. (2007)
778 Equilibration scales in silicic to intermediate magmas - Implications for experimental
779 studies. Journal of Petrology, 48, 1955–1972.
780 Scaillet, B., Holtz, F., and Pichavant, M. (2016) Experimental constraints on the formation of
781 silicic magmas. Elements, 12, 109–114.
782 Schaller, T., Dingwell, D.B., Keppler, H., Knöller, W., Merwin, L., and Sebald, A. (1992)
783 Fluorine in silicate glasses: A multinuclear magnetic resonance study. Geochimica et
784 Cosmochimica Acta, 56, 701–707.
785 Schipper, C.I., Castro, J.M., Tuffen, H., James, M.R., and How, P. (2013) Shallow vent
786 architecture during hybrid explosive-effusive activity at Cordón Caulle (Chile, 2011-12):
787 Evidence from direct observations and pyroclast textures. Journal of Volcanology and
788 Geothermal Research, 262, 25–37.
789 Schipper, C.I., Castro, J., Kennedy, B., Christenson, B., Aiuppa, A., Alloway, B., Forte, P.,
790 Seropian, G., and Tuffen, H. (2019) Halogen (Cl, F) release during explosive, effusive, and
791 intrusive phases of the 2011 rhyolitic eruption at Cordón Caulle volcano (Chile). Volcanica,
792 2, 73–90.
793 Schmidt, B.C., and Behrens, H. (2008) Water solubility in phonolite melts : Influence of melt
794 composition and temperature. Chemical Geology, 256, 259–268.

795 Signorelli, S., and Carroll, M.R. (2002) Experimental study of Cl solubility in hydrous alkaline
796 melts: Constraints on the theoretical maximum amount of Cl in trachytic and phonolitic
797 melts. Contributions to Mineralogy and Petrology, 143, 209–218.
798 Spilliaert, N., Métrich, N., and Allard, P. (2006) S-Cl-F degassing pattern of water-rich alkali
799 basalt: Modelling and relationship with eruption styles on Mount Etna volcano. Earth and
800 Planetary Science Letters, 248, 772–786.
801 Swanson, S.E., and Fenn, P.M. (1992) The effect of F and Cl on the kinetics of albite
802 crystallization: a model for granitic pegmatites? Canadian Mineralogist, 30, 549–559.
803 Thomas, R.W., and Wood, B.J. (2021) The chemical behaviour of chlorine in silicate melts.
804 Geochimica et Cosmochimica Acta, 294, 28–42.
805 Tribaudino, M., Mantovani, L., Bersani, D., and Lottici, P.P. (2012) Raman spectroscopy of
806 $(Ca,Mg)MgSi_2O_6$ clinopyroxenes. American Mineralogist, 97, 1339–1347.
807 von Aulock, F.W., Kennedy, B.M., Schipper, C.I., Castro, J.M., E. Martin, D., Oze, C., Watkins,
808 J.M., Wallace, P.J., Puskar, L., Bégué, F., and others (2014) Advances in Fourier transform
809 infrared spectroscopy of natural glasses: From sample preparation to data analysis. Lithos,
810 206–207, 52–64.
811 Webb, S.L., Murton, B.J., and Wheeler, A.J. (2014) Rheology and the Fe^{3+}-chlorine reaction in
812 basaltic melts. Chemical Geology, 366, 24–31.
813 Webster, J.D., and De Vivo, B. (2002) Experimental and modeled solubilities of chlorine in
814 aluminosilicate melts, consequences of magma evolution, and implications for exsolution of
815 hydrous chloride melt at Mt. Somma-Vesuvius. American Mineralogist, 87, 1046–1061.
816 Webster, J.D., Vetere, F., Botcharnikov, R.E., Goldoff, B., McBirney, A., and Doherty, A.L.
817 (2015) Experimental and modeled chlorine solubilities in aluminosilicate melts at 1 to 7000
818 bars and 700 to 1250 °C: Applications to magmas of Augustine Volcano, Alaska. American
819 Mineralogist, 100, 522–535.
820 Webster, J.D., Baker, D.R., and Aiuppa, A. (2018) Halogens in Mafic and Intermediate-Silica
821 Content Magmas. In D.E. Harlov and L.Y. Aranovich, Eds., The Role of Halogens in
822 Terrestrial and Extraterrestrial Geochemical Processes pp. 307–430. Springer-Verlag.
823 Wyllie, P.J., and Tuttle, O.F. (1961) Experimental investigation of silicate systems containing
824 two volatile components; Part 2, the effects of NH_3 and HF, in addition to H_2O on the
825 melting temperatures of albite and granite. American Journal of Science, 259, 128–143.

——— (1964) Experimental investigation of silicate systems containing two volatile components. Part 3. The effects of SO_3, P_2O_5, HCl and Li_2O, in addition to water on the melting temperatures of albite and granite. American Journal of Science, 262, 930–939.

Zeng, Q., and Stebbins, J.F. (2000) Fluoride sites in aluminosilicate glasses: High-resolution 19F NMR results. American Mineralogist, 85, 863–867.

Zhang, Y. (2010) Diffusion in Minerals and Melts: Theoretical Background. Reviews in Mineralogy and Geochemistry, 72, 5–59.

Zimova, M., and Webb, S. (2006) The effect of chlorine on the viscosity of Na_2O-Fe_2O_3-Al_2O_3-SiO_2 melts. American Mineralogist, 91, 344–352.

Zimova, M., and Webb, S.L. (2007) The combined effects of chlorine and fluorine on the viscosity of aluminosilicate melts. Geochimica et Cosmochimica Acta, 71, 1553–1562.

Figure captions

Figure 1: Backscattered images of experimental run products. **(a)** Detailed view of sample 15X showing the spherulitic aggregation of elongate crystals. **(b)** + **(c)** The halogen-bearing and halogen-depleted control experiments 33X and 34X (both ~30 hours) illustrating the strong contrast in crystallinity. **(d)** Sample 26X illustrating the lack of one sharp transition from crystal-free to crystal-bearing glass. **(e)** Sample 7X (zero-time) showing uniformly crystalline upper half, corresponding to the initially halogen-poor aliquot.

Figure 2: **(a)** – **(c)** Compositional maps of sample 18X. Concentrations of Ca, Fe and Mg are significantly enriched in the crystal phases. Units of intensity correspond to counts (cts). Maps showing the concentrations of other components in this area are provided in Figure S1. **(d)** Raman spectrum of a crystal in sample 24X (bold line). Augite reference spectrum (thin grey line) from the Raman data repository (Lafuente et al. 2015). Intensities in arbitrary units.

Figure 3: Halogen and major element concentration profiles of sample 4X (100 MPa – 950 °C – 15840 s) **(a)** Section of a concentration profile of F and Cl. The diagram is scaled to match the backscattered image in **(b)** showing an enlargement of the very sample. **(c)** Diagram showing the major element concentration of the same section of the profile as in (a). SiO_2 concentration is referenced to the secondary y-axis. The white/black dashed lines mark the inferred diffusion interface at the start of the experiment and the orange dashed lines mark the concentration and position at the transition to crystal-bearing melt. Orange data-points are used to calculate the transition concentration c_{liq} for F and Cl, respectively. The grey lines in (a) are fits calculated with the equation for diffusion between two semi-infinite half spaces (Crank 1975).

Figure 4: **(a)** F and Cl concentration at the point of transition from crystal-bearing to crystal-free melt (c_{liq}) at the different experimental liquidus-temperatures. **(b)** Depression of the liquidus relative to the different experimental liquidus concentrations. ΔT is calculated based on a halogen-free liquidus temperature of 990 °C. Small open symbols represent data averaged from the 4 points closest to the interface and larger solid symbols represent data from analysis along the dissolution front. Error bars on symbols illustrate the standard deviation of the values used to calculate the average concentration.

Figure 5: Fitted halogen concentration profiles of sample 15X. Grey lines show the fitted solution to diffusion equation (1).

879 **Figure 6:** Relation between the observed drop in liquidus temperature based on the halogen-poor
880 liquidus of 990 °C and the sum of c_{liq} of F and Cl (mol%). The dashed line indicates linear
881 regression for the sum of F and Cl concentrations. The regression line involves all data of both
882 approaches to determine c_{liq}. Small open symbols represent data averaged from the 4 points
883 closest to the interface and larger solid symbols represent data from analysis along the
884 dissolution front. Error bars on symbols illustrate the standard deviation of the values used to
885 calculate the average concentration.

886

887

888

889 **Tables**

890

891 **Table 1**: Major element composition of synthesized glasses in wt%. See text for details.

	CC1	CC2	*Puy av.* [b]
F	0.87 (4)	0.06 (3)	-
Cl	0.36 (1)	0.06 (1)	-
SiO_2	65.8 (5)	66.4 (6)	69.9 (1)
TiO_2	0.63 (2)	0.63 (2)	0.70 (3)
Al_2O_3	13.7 (2)	13.9 (3)	14.4 (1)
FeO(tot)	3.4 (3)	3.5 (3)	4.1 (1)
MnO	0.11 (3)	0.10 (3)	0.11 (1)
MgO	0.58 (5)	0.5 (2)	0.54 (5)
CaO	2.00 (2)	1.8 (4)	2.24 (4)
Na_2O	7.6 (2)	7.7 (3)	5.16 (7)
K_2O	2.37 (5)	2.43 (6)	2.76 (2)
LOI	-	-	0.34 (6)
Total	96.93[a]	97.02[a]	100.25

[a] Totals of CC1 and CC2 are corrected for stoichiometric oxygen, calculated by the EPMA matrix correction process.
[b] XRF data from Castro et al. (2013); composition of the starting material used for synthesis of CC1 and CC2.

892

893

894 **Table 2**: Conditions and results of all experiments (P = 100 MPa).

sample	T (°C)	t (s)	H_2O[a] (wt%)	liquidus concentration c_{liq}					
				profile [b]			diss. front [c]		
				F (wt%)	Cl (wt%)	F+Cl (mol%)	F (wt%)	Cl (wt%)	F+Cl (mol%)
17X	925	92280	3.62	-	-	-	-	-	-
26X	940	53640	3.66	0.52 (4)	0.23 (1)	0.034 (2)	0.51 (3)	0.24 (1)	0.034 (2)
4X	950	15840	3.58	0.48 (3)	0.21 (2)	0.031 (2)	0.44 (3)	0.19 (1)	0.029 (2)
6X	950	37860	3.97	0.41 (1)	0.17 (2)	0.026 (1)	-	-	-
7X	950	0	3.87	0.50 (7)	0.24 (3)	0.033 (5)	-	-	-
18X	960	15960	3.50	0.41 (3)	0.18 (3)	0.027 (2)	0.41 (3)	0.18 (2)	0.026 (2)
23X	960	21180	3.58	0.43 (2)	0.16 (2)	0.027 (2)	0.42 (2)	0.16 (1)	0.027 (2)
25X	968	15780	3.53	0.35 (3)	0.16 (2)	0.023 (2)	0.39 (3)	0.17 (2)	0.025 (2)
15X	975	8520	3.68	0.20 (3)	0.07 (1)	0.012 (2)	0.19 (1)	0.07 (1)	0.012 (1)
24X	975	10320	3.57	0.27 (5)	0.09 (3)	0.017 (3)	0.26 (2)	0.09 (1)	0.016 (1)
22X	990	3960	3.70	-	-	-	-	-	-
33X	950	108660	3.39	-	-	-	-	-	-
34X	950	108660	3.49	-	-	-	-	-	-

[a] H_2O initially added to the capsule; considered maximum value.
[b] calculated from the 4 points of the concentration profile which are closest to the dissolution front.
[c] calculated from profiles measured along the dissolution front.

895

Fig. 1

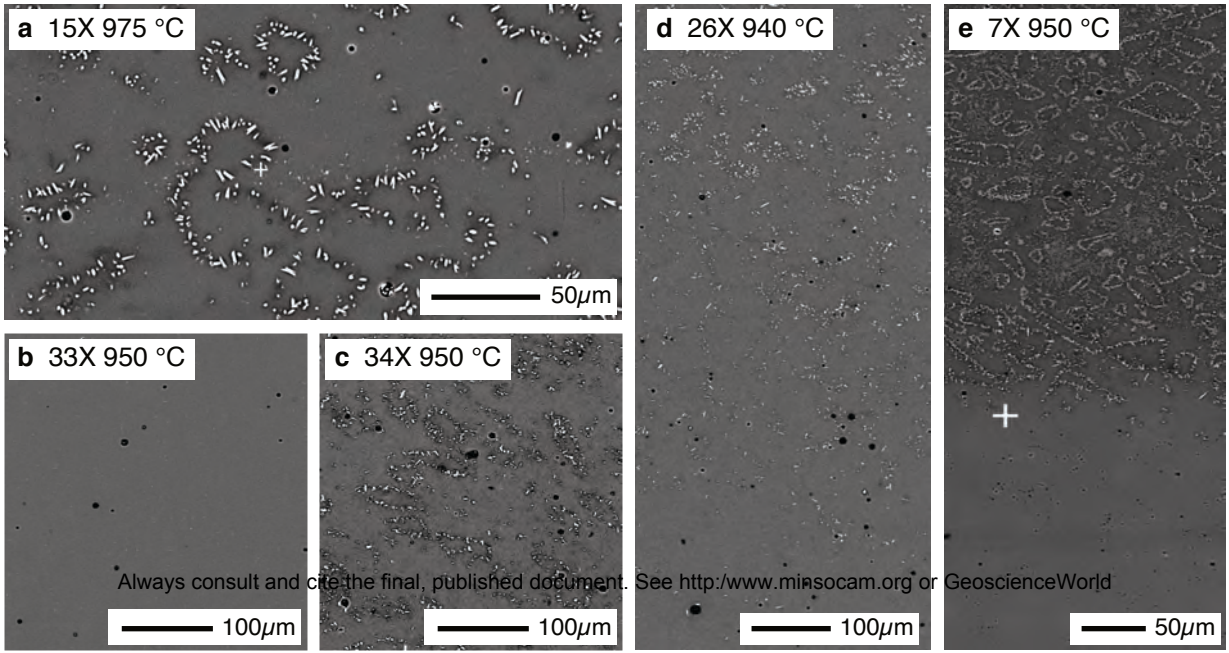

This is the peer-reviewed, final accepted version for American Mineralogist, published by the Mineralogical Society of America.
The published version is subject to change. Cite as Authors (Year) Title. American Mineralogist, in press.
DOI: https://doi.org/10.2138/am-2022-8120. http://www.minsocam.org/

Fig. 2

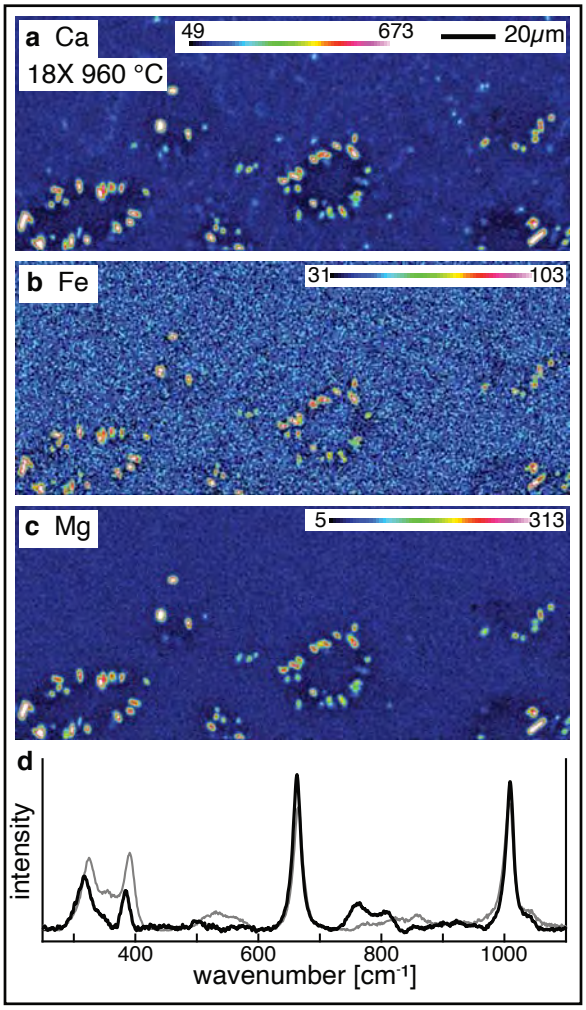

This is the peer-reviewed, final accepted version for American Mineralogist, published by the Mineralogical Society of America.
The published version is subject to change. Cite as Authors (Year) Title. American Mineralogist, in press.
DOI: https://doi.org/10.2138/am-2022-8120. http://www.minsocam.org/

Fig. 3

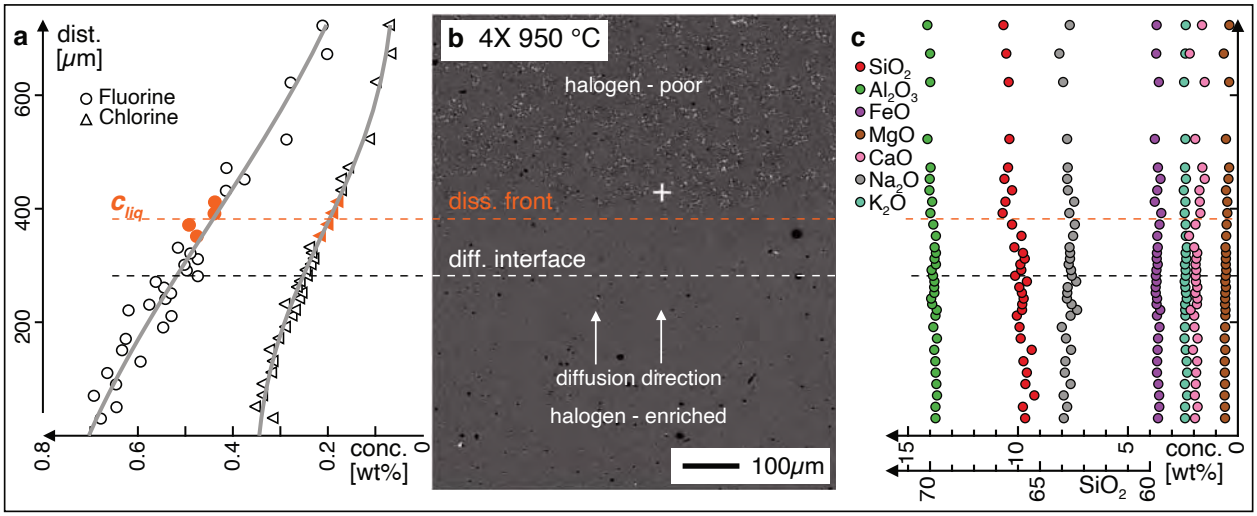

This is the peer-reviewed, final accepted version for American Mineralogist, published by the Mineralogical Society of America.
The published version is subject to change. Cite as Authors (Year) Title. American Mineralogist, in press.
DOI: https://doi.org/10.2138/am-2022-8120. http://www.minsocam.org/

Fig. 4

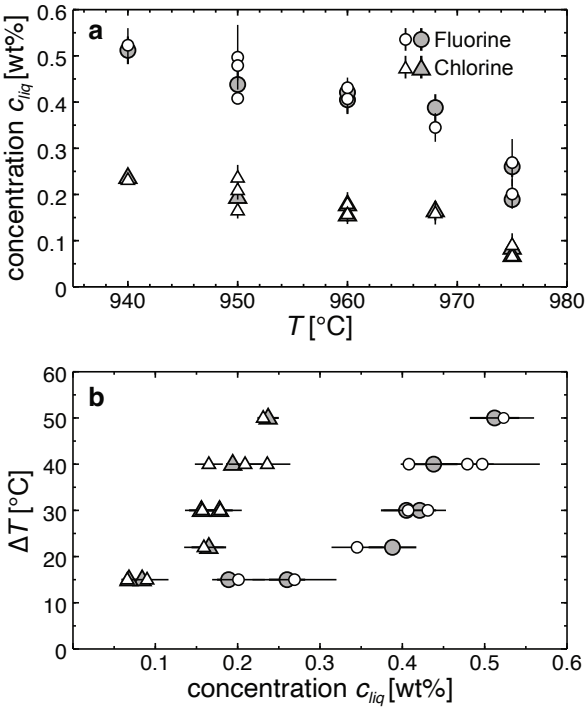

Fig. 5

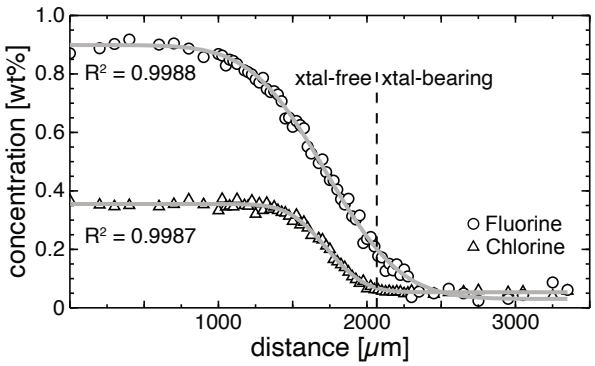

This is the peer-reviewed, final accepted version for American Mineralogist, published by the Mineralogical Society of America.
The published version is subject to change. Cite as Authors (Year) Title. American Mineralogist, in press.
DOI: https://doi.org/10.2138/am-2022-8120. http://www.minsocam.org/

Fig. 6